crystals

MDPI

Review

Quaternary Misfit Compounds—A Concise Review

Sokhrab B. Aliev † **and Reshef Tenne** *

Department of Materials and Interfaces, Weizmann Institute, Rehovot 76100, Israel; yosef.elion@weizmann.ac.il
* Correspondence: reshef.tenne@weizmann.ac.il
† Now, Yosef Elion.

Received: 21 April 2020; Accepted: 9 May 2020; Published: 1 June 2020



Abstract: Misfit layered compounds (MLCs) have been studied in the literature for the last 40 years. They are generally made of an alternating sequence of two monolayers, a distorted rocksalt structure, and a hexagonal layered compound. In a typical MLC, the *c*-axis is common to the two monolayers and so is one of the axes in the layer plan. However, the two compounds are non-commensurate along at least one axis, and the ratio between the two axes is an irrational number making the MLC a non-stoichiometric compound. The two main families of MLC are those based on metal dichalcogenides and CoO_2 as the hexagonal layered compound. Traditionally, ternary MLCs were prepared and studied, but some quaternary and multinary MLC minerals have been known for many years. Over the last few years, interest in MLCs with four and even larger number of atoms has grown. Doping or alloying of a ternary MLC permits precise control of the charge carrier density and hence the electrical, thermoelectric, catalytic, and optical properties of such compounds. In this short review, some of these developments will be discussed with the main emphasis put on quaternary MLC nanotubes belonging to the chalcogenide series. The synthesis, structural characterization, and some of their properties are considered. Some recent developments in quaternary cobaltite MLCs and recent studies on exfoliated MLCs are discussed as well.

Keywords: misfit compounds; inorganic nanotubes; metal dichalocgenides; cobaltites

1. Introduction

Misfit layered compounds (MLCs) are (2D) non-stoichiometric materials comprising two interpenetrating sublattices differing in at least one of their lattice parameters [1,2]. These layers are made of a stacking of a distorted rocksalt slab attached to a layered material with hexagonal structure. The layers form a superstructure with periodically alternating atomic layers. To date, the most studied structures are misfit materials based on either metal dichalcogenides or the layered cobaltites, which will only briefly be mentioned here. The metal dichalcogenide-based MLCs are made of layers with the general formula $[(MX)_{1+y}]_m[TX_2]_n$ (where M = Sn, Pb, Bi, Sb, Y, rare earths; T = Sn, Nb, Ta, Ti, V, Cr, and X = S, Se, Te) [3–8] and m,n are integers. The parameter y represents the deviation from stoichiometry of the MLC. Figure 1 presents a schematic drawing of a chalcogenide-based MLC lattice. For the sake of brevity, these MLCs are designated as $MX\text{-}TX_2$ or $(MX)_m\text{-}(TX_2)_n$.

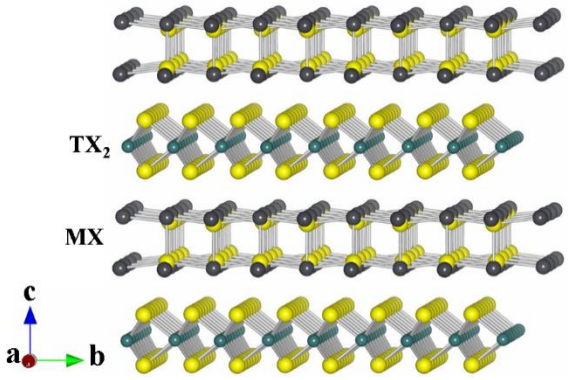


Figure 1. Schematic representation of the structure of misfit layered compounds (MLCs) $(MX)_{1+y}TX_2$ viewed from the [100] direction. Green, gray, and yellow full circles are T, M, and X atoms, respectively. The MX layer has a (distorted) rocksalt structure while the TX_2 is a layer with hexagonal lattice.

In general, the *c*- and *b*-axes are common to the two units, while the *a*-axes differ between the two sublattices. The ratio between the two *a*-axes, i.e., a_{MX}/a_{TX2}, is an irrational number, therefore, the MLC is non-stoichiometric. The volume of the unit cells of the two sublattices is different and the hyperstoichiometry parameter y is determined by $1 + y = 2\, a_{TX2}/a_{MX}$, $0.08 \leq y \leq 0.30$. In common with other layered compounds (2D materials), the chemical bonds within the layer are covalent. The layers are stacked together by weak van der Waals forces, which are at least one order of magnitude weaker than the intralayer covalent bonds. MLCs can be also viewed as intercalation compounds, whereby a single layer of a compound with distorted rocksalt structure and low work function, like LaS, is intercalated in the galleries between each of the two adjacent layers of the hexagonal layered compound, like TaS_2, which is a Lewis base (electron acceptor). Consequently, the stability of the MLC lattice is improved by partial charge transfer from the MX slab to the TX_2 one. Owing to their unusual structure, MLCs make a very special class of materials with interesting properties, which have so far been only succinctly studied [6,9]. Due to their uncommon structure, substantial efforts were directed in recent years towards the synthesis of nanostructures and complex MLC architectures as a first step in the study of this highly perspective class of materials. The alloying of the cation site (M) in the rocksalt structure, the T site in the hexagonal lattice, or the anion sites X was investigated over the last few years, leading to intriguing quaternary materials, which are discussed hereby. As is often the case in materials science, the early work on MLCs focused on minerals available in nature [3], which promoted the research into synthetic MLCs and their nanostructures further.

Another type of MLC, which were studied quite intensively and are described only briefly here, are the cobaltites. One such quaternary MLC series has the general formula $AO\text{-}(MO)_m\text{-}AO\text{-}CoO_2$ with m = 1 or 2 (M= Co, Bi, etc.; A= Ca, Sr, etc.), discovered by Raveau and co-workers [10]. The structure of the misfit compound $(Ca_2CoO_{3.34})_{0.614}CoO_2$ or $Ca_3Co_4O_9$ was studied in [11]. These misfit compounds are represented generally by the formula $(M_mA_2O_{2+m})_qCoO_2$. The misfit parameter q is determined by the ratio of the mutually incommensurate *b*-axes of the two sublattices of the distorted rocksalt structure $M_mA_2O_{2+m}$ and the CoO_2 [12,13]. The misfit cobaltites were investigated in relation to their favorable thermoelectric properties. For example, alloying the rocksalt lattice with bismuth, which partially substitutes the original calcium atoms in the rocksalt structure, led to improved thermoelectric behavior [14]. In another work, iron and lanthanum alloying of the MLC $Ca_3Co_4O_9$ led to efficient phonon scattering and improved thermoelectric power generation at elevated temperatures [15]. These studies highlight the importance of substitutional doping and alloying for tuning the properties of misfit compounds. The quaternary MLCs of the cobaltite series will be briefly described in the context of their potential applications in high temperature thermoelectric power conversion, rechargeable batteries, and electrocatalysis.

Interestingly, doping and alloying of chalcogenide-based MLCs of the type $[(MX)_{1+y}]_m[TX_2]_n$ by foreign atoms, has been scarcely investigated until very recently. One important exception is

the class of naturally occurring MLCs known under the general name Franckeites, like the mineral $Pb_{4.6}Ag_{0.2}Sn_{2.5}Fe_{0.8}Sb_2S_{12.6}$ [16] and compounds with the general formula $(M_1M_2S)_{2(1+y)}TS_2$, like $[(Pb, Sb)S]_{2.28}NbS_2$, which were studied in the early 90s of the last century [17].

In the present paper, the structure and some properties of chalcogenide-based misfit structures made of four elements and published recently are reviewed. The relationship between the chemistry of such compounds and their nanotubular structures is deliberated, as well as some of their optical and electrical properties. In common with recent trends in 2D materials research, exfoliation of the bulk material into single or a few layers MLC has been explored in recent years. Furthermore, in parallel with graphite and WS_2, MLC nanotubes have been prepared and studied in recent years, which are discussed below.

Inspired by the discovery of carbon nanotubes in 1991 and the analogy between graphite and inorganic layered compounds (2D materials), Tenne and co-workers proposed that nanoparticles of WS_2 and subsequently MoS_2 are unstable against folding and seaming forming hollow polyhedral (fullerene-like) nanoparticles and nanotubes [18–20]. This concept paved the way for much research and nanotubes from numerous 2D compounds were subsequently synthesized and studied by various research groups and in silico.

Nanotubes from the (ternary) misfit compound $(SnS)_{1.29}SnS_2$ were obtained serendipitously, upon laser ablation of SnS_2 [21]. This work was later systematized via chemical vapor transport (CVT) growth of similar nanotubes [22] and from numerous other ternary MLCs [2]. The main driving force for the formation of MLC nanotubes stems from the strain between the two MX and TX_2 subunits stimulated by the dissimilar lattice constant (usually the *a*-axis) of the two structures. Relaxing this strain in the high temperature vapor phase leads to folding of the MLC layers. Concomitantly, another driving force for the formation of nanotubes comes into action. This stimulus is associated with the minimization of the chemical energy stored in the unsaturated rim atoms in the MLC nanocluster, which was discussed previously in relation to WS_2 (MoS_2) nanotubes [18–20]. To minimize the chemical energy stored in the dangling bonds of the rim atoms, the MLC sheets further fold and finally seam and heal the dangling bonds, forming thereby nanotubes [23]. The strain energy is more than compensated by healing of the dangling bonds of the rim atoms.

The vast majority of MLCs in the literature are made of three elements (ternary MLC). However, over the last five years or so, quaternary MLC alloys emerged as an interesting research topic. They are generally obtained by partial substitution of one of the elements in the ternary MLC lattice leading to compounds with unique structures and properties. Such materials are called quaternary MLCs or MLC alloys. While a growing number of publications were devoted to quaternary crystals and films, others dealt with nanotubes made of quaternary MLC. The partial replacement of a cation or anion in the MLC network provides a new gauge to control the amount of strain and charge transfer between the (distorted) rocksalt layer (electron donor) and the hexagonal "host" (acceptor). The amount of charge transfer between the two layers influences the interlayer forces, the stability of the MLC, and its electronic and optical properties, among others. For instance, LaS is a Lewis acid (electron donor) and is in excess with respect to the TaS_2 in the $(LaS)_{1.14}TaS_2$ lattice [24]. The partial charge transfer from the LaS goes to the half-filled $5d_z^2$ levels of the (semimetallic) TaS_2. Furthermore, the extra negative charge of the LaS can be compensated via lanthanum vacancies, antisites, etc. Substitution of the La atom by the divalent strontium (Sr_{La}) atom in the MLC lattice has been discussed in a few earlier works, like [25]. This substitution reduces the charge imbalance and can promote other defects, if present in excess of 15 at % in the MLC lattice. In yet another work [26], the effect of Sr substitution of La atoms on the electrical properties of the misfit compound $La_{1.17-x}Sr_xVS_{3.17}$ was elucidated. In particular, the electronic conductivity, which was dominated by free electrons, decreased with the addition of vanadium atoms up to $x = 0.17$, where it became a Mott insulator. Increasing the strontium content beyond this value, the conductivity went up due to the increase in the free-hole density. Indeed, the material became a metal at x larger than 0.3.

Table 1 summarizes some of the different synthetic strategies that were used for the growth of various quaternary misfit compounds, which are the focus of the present manuscript.

Table 1. Summary of the data for quaternary misfit layered compounds: synthesis technique, elements and morphology of the MLCs.

Compound	Precursor	Growth Technique	Morphology of the Quaternary MLC	Reference
$Pb_{4.6}Ag_{0.2}Sn_{2.5}Fe_{0.8}Sb_2S_{12.6}$	Mineral-Franckeite	Mineral	Flakes	[16]
$[(Pb, Sb)S]_{2.28}NbS_2$	Pb, Sb, Nb, S	Chemical vapor transport	Flakes	[17]
$Sr_xLa_{(1-x)}S\text{-}TaS_2$	La, Sr, Ta, S	Chemical vapor transport	Nanotubes and flakes	[27]
$LaS\text{-}Nb_xTa_{(1-x)}S_2$	La, Ta, Nb, S, $TaCl_5$	Chemical vapor transport	Nanotubes and flakes	[28]
$LnS(Se)\text{-}TaS_2(Se)$	Ta, Ln = La, Ce, Nd, Ho; S, Se, and $TaCl_5$	Chemical vapor transport	Nanotubes and flakes	[29]
$Ln_xLa_{1-x}S\text{-}TaS_2$	Ln = Pr, Sm, Ho, and Yb	Chemical vapor transport	Nanotubes and flakes	[30]
$Y_xLa_{1-x}S\text{-}TaS_2$	La, Y, S, Ta	Chemical vapor transport	Nanotubes and flakes	[31]
$(SnSe)_{1.16-1.09}Nb_xMo_{1-x}Se_2$	Sn, Nb, Mo, Se	Compositionally modulated elemental reactants synthesis	Films	[32]
$[(Bi_{0.4}Nd_{0.6})S]_{1.25}CrS_2$ and $[Pb_{0.5}Nd_{0.5}Se]_{1.15}(NbSe_2)_2$	Nd, Cr, S, Se, Bi_2S_3	Chemical vapor transport	Flakes	[33]
$Bi_2M_3Co_2O_y$ with M = Ca, Sr, Ba	Bi_2O_3,$CaCO_3$, Co_3O_4	Flux synthesis	bulk	[34]
$(Bi_2Ca_2O_4)_qCoO_2$	Bi_2O_3,$CaCO_3$, Co_3O_4	Flux synthesis	bulk	[35]
$(SnS)_{1.2}(Co_{0.02}Ti_{0.98}S_2)_2$	Sn, Ti, S and Co	Chemical vapor transport	bulk	[36]
Na: $PbNbS_3$; $PbNb_2S_5$	Na, Pb, Nb, S	Electrochemical intercalation	bulk	[37]
$Bi_2Sr_2Co_2O_{8+\delta}$	Bi, Sr, Co, O	Exfoliation of bulk crystal	Exfoliated sheets	[38]

2. Synthesis and Structural Elucidation of Nanotubes from Quaternary MLC

2.1. Prelude

Generally, complexity does not necessarily mean addressing a penetrating question, but is certainly a likely option. In the following work a few examples of nanotubes and films prepared from quaternary MLC nanotubes, are described in order to address what appears to be an important structural or physico-chemical topic. Density functional theory (DFT) calculations made an essential contribution to addressing some of the questions. Regrettably though, physical measurements of MLC nanotubes, such as optical and transport properties, are rather limited, so far. Specifically, the immense potential for device physics, particularly at low temperatures, has not been embraced so far by the scientific community. This limited knowledge notwithstanding, quaternary MLC nanotubes (and films/bulk crystallites) are an interesting if not enticing research object, as shown below. Generally, MLC nanotubes belonging to the family $LnS\text{-}TaS_2$ (Ln = rare-earth atom), and the quaternary nanotubes thereof, were found to be very sensitive to oxidation. This chemical reactivity is not unexpected, given the great chemical stability of Ta_2O_5 and the respective Ln_2O_3 compounds. In some of the earlier studies, the quality of the analysis was compromised due to surface oxidation of the nanotubes. More recently, however, extensive efforts to prevent the oxidation and degradation of the nanotubes resulted in much cleaner surfaces and more reliable analysis of their structure and properties.

2.2. Synthesis

Chemical vapor transport (CVT) and physical vapor transport (PVT) were found to be successful strategies for the synthesis of a series of quaternary MLC nanotubes, however the yield of the nanotubes varied from one compound to the other and was far below unity. The product was mixed with flakes,

usually with the same composition. The general procedure included adding a mixture of the elements and the binary metal sulfides in the presence of catalytic amounts of $TaCl_5$ into a quartz ampule. The transport agent $TaCl_5$ is a well-known catalyst (growth promoter) in such transport reactions. A high temperature annealing (600–900 °C) was carried out for several hours in order to induce a chemical reaction and homogenize the product. Subsequently, the ampule was heated under a given temperature gradient for a few hours. The powder was placed in the hot zone of the heated ampule, typically between 850–900 °C. The other side of the ampule was held at 250–400 °C. In several cases, the powder was transported from the hot to the cold zone. Upon reassembling into clusters in the colder zone, the strain between the rocksalt and hexagonal layers relaxed by folding the MLC slab into nanotubes or else nanoscrolls. In some other syntheses the heated powder remained at the hot edge and the nanotubes were obtained as a result of a local recrystallization. In the first part of this review, the work on quaternary MLC nanotubes is discussed in some detail.

2.3. Sr-Substituted LaS-TaS_2 Nanotubes

Substitution of the strontium atom in the LaS-TaS_2 nanotube lattice raises questions not relevant for flakes, like the relationship between charge imbalance and the strain, etc., which was addressed in [27]. Tubules (and flakes) of the misfit compounds $Sr_xLa_{(1-x)}S$-TaS_2 with ascending Sr concentrations were prepared. The chemical vapor transport (CVT) technique was used for the synthesis. The precursors La, SrS, Ta, and S were taken in the molar proportion 1:1:3 (La + Sr)/Ta/S and mixed with a catalytic amount of $TaCl_5$ and were annealed in two steps. In the first step the ampoule was submitted to a thermal gradient of 390 °C (bottom edge where the powder was placed) and ≈ 800 °C (upper edge). After one hour the ampoule was moved inside the furnace and exposed to an opposite temperature gradient of 860 °C at the lower edge (were the powder was placed) and ≈390 °C at the upper edge. This second step lasted 6 h. The Sr content in the precursor is expressed as at %. For example, 10 at % is equivalent to $(Sr_{0.1}La_{0.9}S)_{1.14}TaS_2$ or for simplicity $Sr_{0.1}La_{0.9}S$-TaS_2. Nanotubes and flakes of the MLC alloy $Sr_xLa_{1-x}S$-TaS_2 with varying Sr compositions (at % Sr: 10%, 20%, 40%, 60%) were prepared. Correspondingly, the La atom content in the precursor was reduced from 90 to 40 at %. No nanotubes could be observed beyond 60% Sr, and hence, compositions richer in Sr were not prepared and analyzed in this study.

Scanning electron microscope (SEM) analysis showed that the nanotubes were formed in all the selected compositions (Figure 2). The yield of the nanotubes decreased with increasing Sr content. A transmission electron microscope (TEM) image and selected area electron diffraction (SAED) pattern of a 10 at % nanotube are presented in Figure 3. The SAED of a nanotube containing 60 at % Sr in the precursor contained six pairs of spots corresponding to the (10.0) (zig-zag) planes of the TaS_2 unit with a *d*-spacing of 2.82 Å. Another six pairs, which can be indexed to the (11.0) (armchair) planes (marked with red circles) of TaS_2 with a spacing of 1.63 Å were also observed (Figure 3b). This observation confirmed the presence of two folding vectors for the TaS_2 in the investigated nanotube. Eight pairs of spots at 3.97 Å and 2.04 Å were also observed (marked by green circles), which could be indexed to the (110) and (220) planes of LaS, respectively. The multiplicity factor of these planes is four, therefore the presence of two folding vectors could be confirmed for the LaS lattice as well. The existence of two different azimuthal orientations of the nanotube walls with respect to the growth axis can be attributed to the existence of yet another strain relaxation mechanism in such quaternary nanotubes, which did not occur in the ternary LaS-TaS_2 nanotube. This unexpected strain relaxation mechanism should be studied further in future research. Clearly then, the elastic strain in the Sr-substituted LaS-TaS_2 MLC tubes is relaxed via the multiplicity of lattice orientations in the nanotubes. In contrast to that, tubular LnS-TaS_2 (Ln = rare earth) was found to have one single orientation in the majority of analyzed cases with the common *b*-axis parallel to the nanotube axis (see Figure 3c).

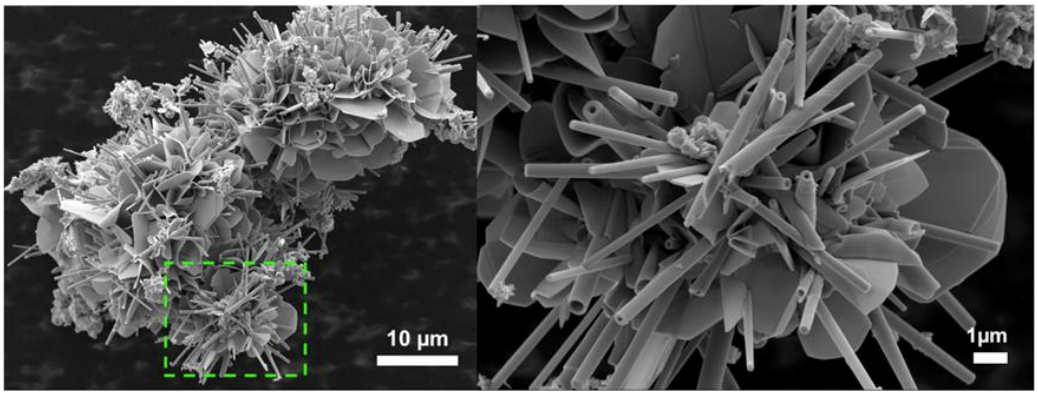


Figure 2. SEM images (two different magnifications) of $La_xSr_{1-x}S$-TaS_2 powder prepared from 10 atom % Sr (90 atom % La) in the precursor. Tubular structures and conical nanoscrolls along with sheet-like morphology (flakes) are visible (adopted from [27]).

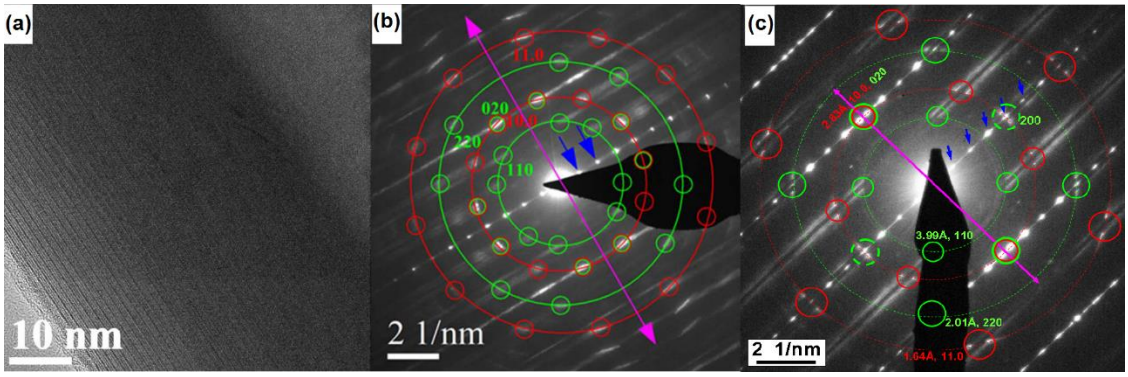


Figure 3. (**a**) High resolution transmission electron microscope (HRTEM) image of a $Sr_xLa_{1-x}S$-TaS_2 (Sr 60 at %) tube. (**b**) Selected area electron diffraction (SAED) showing the orientation relationship between the $Sr_xLa_{1-x}S$ layers (green) and the TaS_2 layers (red). The tube axis is represented by the pink double arrow, and the basal reflections are marked with blue arrows (adopted from [27] courtesy of Dr. L.F. Deepak). (**c**) SAED of a LaS-TaS_2 nanotube (adopted from [24]) with the *b*-axis [10.0]|||[020] parallel to the tube axis.

The splitting of the spots indicates the chiral nature of the nanotube. The chiral angles calculated from the splitting of the spots, *hk*.0 of LaS and TaS_2, were ≤3°. Furthermore, it was observed that the (020) spot of LaS coincides with the (10.0) of TaS_2, even though they are not parallel to the nanotube axis, marked as a pink double arrow. This result shows that the *b*-axis is common to the two sublattices. The SAED consists of six pairs (red circles) of the TaS_2 layer with its *b*-axis [10.0] pointing in the axial (growth) direction of the nanotube. Furthermore, there are four pairs of spots diffracted from the (110) plan of the LaS, which are oriented at 45° with respect to the axial direction of the nanotube (green circles). The basal reflections are the spots appearing perpendicular to the nanotube axis (blue arrows). The periodicity along the *c*-axis is ≈1.16 nm (Figure 3a). Furthermore, the interlayer spacing along the *c*-axis was found to increase with ascending strontium content, which is indicative of the weakening interlayer force. Possibly, the charge transfer between the $Sr_xLa_{1-x}S$ and the TaS_2 units is reduced with increasing Sr content (x), weakening thereby the interlayer force holding the MX-TX_2 layers together. DFT calculations confirmed the experimental findings and the stability limit of these alloy nanotubes up to 60 at % Sr.

Analysis of a $Sr_{0.1}La_{0.9}S$-TaS_2 nanotube with high angle annular dark field-scanning TEM image (STEM-HAADF) is shown in Figure 4. Figure 4a presents an overall image of the nanotube, while Figure 4b shows a high resolution STEM-HAADF image of a portion of that nanotube. The bright outer TaS_2 layer is clearly visible, while the two rows of La(Sr) atoms belonging to the $Sr_{0.1}La_{0.9}S$ sublattice

are discernible too. One notes that while some of the $Sr_{0.1}La_{0.9}S$ layers are oriented with their [110] axis with respect to the beam, others are out of focus and are tilted with respect to the [110] zone axis of that layer. This observation conforms well with the SAED analysis (Figure 3b), which indicated two rotation angles for this layer in the nanotube. It can be therefore concluded that the strontium atom substitutes the lanthanum atom in the rocksalt unit and reduces the amount of charge transfer from the MS unit to the TS_2 one.

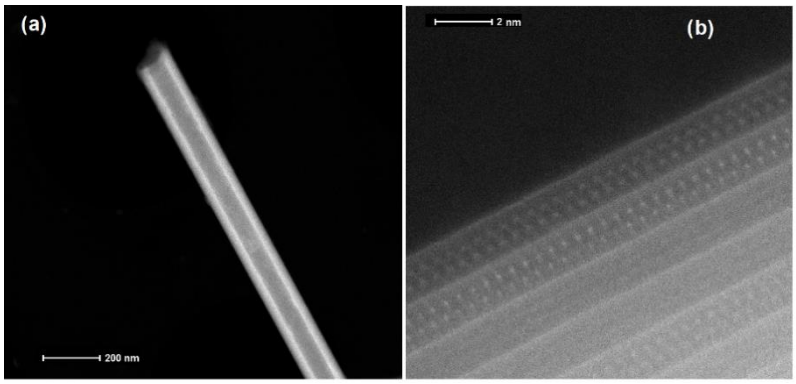


Figure 4. High angle annular dark field-scanning TEM (STEM-HAADF) low resolution images of $Sr_{0.1}La_{0.9}S$-TaS_2 (Sr 10 atom %) nanotubes. (**a**) An overall image of the nanotube and (**b**) high-resolution image of (a) showing that TaS_2 is the outermost layer of the nanotube. The image also shows that some of the $Sr_xLa_{1-x}S$ double layers are oriented with their [110] axis parallel to the beam, while others are out of focus, indicating that they are tilted with respect to the beam (adapted from [27] courtesy of Dr. L.F. Deepak).

2.4. Nb-Substituted LaS-TaS_2 Nanotubes

While both bulk $(LaS)_{1.15}TaS_2$ and $(LaS)_{1.15}NbS_2$ MLC are known in the literature [39], nanotubes of the former are abundant. However, hardly any nanotubes have been obtained from the latter MLC in the CVT process, so far. In order to shed light on this riddle, nanotubes of the quaternary compound $(LaS)_{1.15}Nb_xTa_{1-x}S_2$ with ascending Nb content were prepared [28].

The LaS-$Nb_xTa_{(1-x)}S_2$ nanotubes were obtained using a CVT reaction starting from a mixture of La, Ta, Nb, and S in the presence of a catalytic amount of $TaCl_5$. The powders were mixed in 1:1:3 proportion and placed in a quartz ampule in a glovebox under nitrogen atmosphere in order to prevent the oxidation of the reactants. In each synthesis, a certain percentage of Ta (10 at %, 20 at %, 40 at %, 60 at %, 80 at %, and 90 at %) was replaced by the corresponding molar amount of Nb at % (= 100-at % of Ta). The high-temperature annealing procedure was carried out at 857 °C at the bottom zone and 400 °C at the upper zone of the ampule for 6 h.

As anticipated, the relative abundance of the LaS-$Nb_xTa_{(1-x)}S_2$ nanotubes decreased with ascending Nb content. Also, the Nb content in the nanotubes was found to be a mere few percent up to 60 at % niobium content in the precursor. Beyond that threshold value, the Nb content in the nanotubes increased substantially reaching (on the average) 75 at % when 90 at % Nb (and 10 at % Ta) was used in the precursor.

Indeed, the yield of the nanotubes in the product dropped with increasing niobium content. Particular attention was given to the analysis of the nanotubes produced from 80 at % Nb in the precursor. First, in all the analyzed tubes of this kind the $Nb_xTa_{(1-x)}S_2$ sublattice belonged to the 1T polytype, which is rather uncommon among bulk MLCs of TaS_2 (NbS_2). However, no evidence was obtained for a transition into a charge density wave phase, which is typical for 1T-TaS_2 [40]. Furthermore, in several nanotubes analyzed via energy dispersive X-ray spectroscopy (EDS), the niobium content was not uniform along the nanotube length. Rather it increased (corresponding to a reduced tantalum content) towards the upper end of the tube. This non-uniformity was attributed to the greater volatility of $TaCl_5$ compared to $NbCl_5$, which was depleted from the precursor with

increasing growth time. In accordance with the $Sr_xLa_{(1-x)}S$-TaS_2 nanotubes described above, the SAED showed that the *b*-axis, i.e., the (020) plans of the LaS and the (10.0) axis of the $Nb_xTa_{(1-x)}S_2$, were azimuthally tilted 30° with respect to the growth axis of the tubes. In fact, part of the nanotubes prepared from 80 at % Nb in the precursor exhibited double periodicity (2.25 nm instead of 1.12 nm). This period doubling means that every MS-TaS_2 layer is azimuthally tilted 30° with respect to the adjacent layer in a periodic fashion. Therefore, such nanotube exhibits two kinds of periodicities (superstructure), one typical for any MLC, i.e., the alternating MS and TS_2 layers, and the second emanating from the periodic 30° azimuthal tilting of each two adjacent MS-TS_2 layers. Other nanotubes showed a mixture of single and double periodicity in the radial direction (*c*-axis). Again, this azimuthal variance is indicative of the unique strain relaxation mechanism in alloy MLC nanotubes, which is partially relaxed by having an alternating order of layers. This strain relaxation mechanism is rather uncommon in the ternary MLC nanotubes, where the tube axis coincided with the *b*-axis of the tube.

The LaS-$Nb_xTa_{(1-x)}S_2$ nanotubes prepared from precursors containing up to 60 at % Nb (>40 at % Ta) showed Raman spectra typical for LnS-TaS_2 MLC (see Figure 5). In brief, regardless of the specific compound, a typical spectrum of LnS-TaS_2 MLC consists of two main ranges: 100–150 cm^{-1}, which belongs to the rocksalt (MS) modes, and a 250–400 cm^{-1} range assigned to the TaS_2 slab [41]. Two peaks RS1 (~122 cm^{-1}) and RS2 (~148 cm^{-1}) belong to the antisymmetric and symmetric A_{1g} modes of the rocksalt unit, respectively. The peak in 322–325 cm^{-1} is assigned to the in-plan E_g mode of the TaS_2 and is sensitive to the degree of charge transfer from the LaS to the $Nb_xTa_{(1-x)}S_2$ slab (279 cm^{-1} for pure TaS_2 [24]). The peak in 400 cm^{-1} is assigned to the out of plan A_{1g} mode of the TaS_2. The major changes in the Raman spectra of the 60% (green curve) and 80% (purple curve) nanotubes are probably a manifestation of the structural changes from 2H to 1T of the $Nb_xTa_{(1-x)}S_2$ slab. In general, the Raman spectra of nanotubes with large Nb content were very different from the ones with low Nb content and those of pure LaS-TaS_2 nanotubes. However, the Raman spectra of the MLC tubes with the larger Nb content did not indicate any evidence for charge density wave transition, which is well-established for pure 1T-TaS_2 [42].

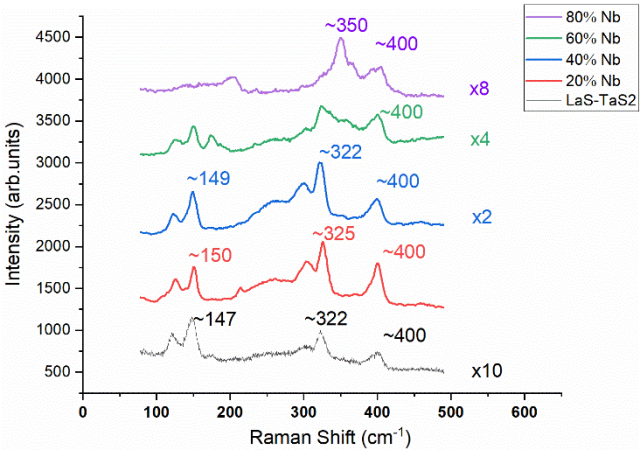


Figure 5. Raman spectra of five different LaS-$Nb_xTa_{(1-x)}S_2$ MLC tubes with different Nb content (adapted from [28]).

In conclusion, the lattice constants *c*/2 and *a* of NbS_2 (5.94 and 3.330 Å, respectively) are smaller compared to those of TaS_2 (6.05 and 3.314 Å). Therefore, the strain between the rocksalt and the hexagonal sublattices in the NbS_2-rich MLC is partially relieved. This partial strain relaxation reduces the driving force for the formation of nanotubes with high niobium content, which may explain the reduced yield of the nanotubes with increasing niobium content in the product.

2.5. Nanotubes from Mixed Sulfur and Selenium MLC

In yet another work, a new class of quaternary chalcogenide-based misfit nanotubes LnS(Se)-TaS_2(Se) (Ln = La, Ce, Nd and Ho) were reported [29]. Ta, Ln (La, Ce, Nd, Ho), S, Se, and $TaCl_5$ powders were mixed in a molar ratio of ~1:1:1.5:1.5:0.1 and sealed in a quartz ampule. The ampule was heated for 4 h at 900 °C in the furnace.

All LnS(Se)-TaS_2(Se) nanotubes exhibited a high degree of crystallinity. The structures appeared to be similar to those of PbS-TaS_2 [43], PbS-NbS_2 [44], LnS-TaS_2, and LaSe-$TaSe_2$ [24] nanotubes. The SAED pattern of the tubes exhibited twelve couples of 11.0 and 10.0 spots of TaX_2, suggesting two folding vectors. In common with the quaternary nanotubes described before, this splitting indicated the existence of two folding vectors for the pseudohexagonal TaS_2(Se) (and the LaS) layers of the nanotube. In several nanotubes this 30° rotation with respect to the growth axis was periodic, and hence double spacing along the *c*-axis (2.3 nm) was observed. In some other nanotubes, regular interlayer spacing of ca. 1.15 nm was recorded and the adjacent layers were either in-phase or rotated 30° with respect to each other layer, but without any specific order.

High-resolution STEM-HAADF analysis of LaS(Se)-$TaS(Se)_2$ nanotubes revealed that the intensity of the selenium and tantalum signals were in-phase with respect to each other, while the lanthanum signal was antiphase with respect to the other two (Figure 6). Generically, tubes with random distribution of the sulfur and selenium atoms in the lattice would have higher entropy and hence lower free energy compared to the situation where each of them is in a different layer of the MLC lattice. Notwithstanding this fact, the electron energy loss spectroscopy in STEM mode (STEM-EELS) analysis showed that the two atoms preferred specific sites in the nanotube lattice, i.e., LaS-$TaSe_2$. This unexpected result could be attributed to the greater affinity of the selenium atom to the hexagonal lattice or the sulfur atom to the rocksalt lattice. Further work is needed in order to clarify this surprising behavior.

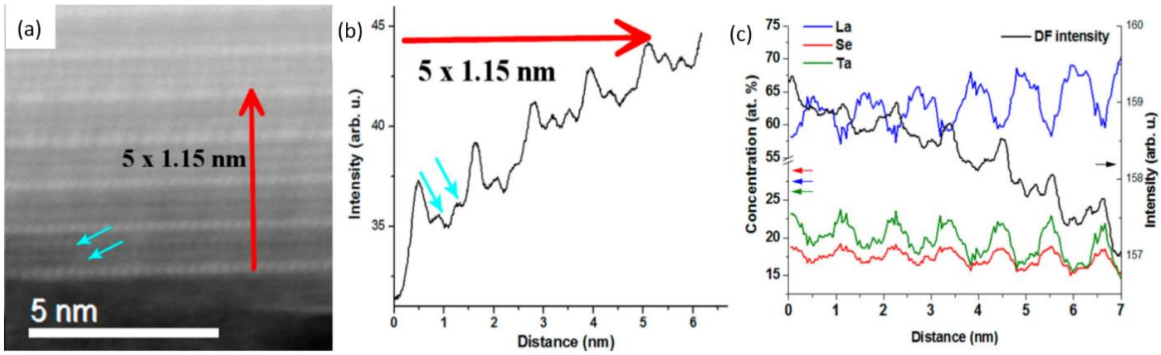


Figure 6. (**a**) High resolution high angle annular dark field (HAADF) mode in STEM of a LaS(Se)-$TaS(Se)_2$ nanotube with the 1.15 nm periodicity of the bright (TaS_2) layers. (**b**) The HAADF intensity profile with the 1.15 nm periodicity of the layers. (**c**) Superposition of the elemental composition obtained from STEM-EELS (electron energy loss spectroscopy) and the STEM-HAADF intensity profile. The blue, red, and green lines correspond to the La, Se, and Ta atomic concentrations, while the black line corresponds to the ADF intensity profile (adapted from [29] with American Chemical Society (ACS) permission; courtesy of Dr. R. Arenal).

Remarkably therefore, in these nanotubes two superstructures of the Ta/La and S/Se coexist for each layer. It remains to be seen how general this trend is in other quaternary tubes of similar composition.

2.6. Quaternary $Ln_xLa_{(1-x)}S$-TaS_2 Nanotubes (Ln = Pr, Sm, Ho, and Yb)

The MLC $(LaS)_{1.11}TaS_2$ hyperstoichiometry is electron rich (metallic-like) and the Fermi level is dominated by the almost fully occupied $5dz^2$ level of the tantalum atom and virtually empty 5*d* level of the lanthanum. In an attempt to increase the yield of the MLC nanotubes, partial substitution of

the La atom with a rare-earth atom was considered, both theoretically and by experiment. From the theoretical viewpoint, two factors could play the main role in this substitution: the size of the rare-earth atom and the density of states near the Fermi level. Clearly, the larger the radius of the rare-earth atom is, the smaller the value of the hyperstoichiometry (y) is and, hence, the excess of electrons in the MS lattice. Since the atomic radius of the rare-earth atoms shrinks with increasing atomic number, this consideration would make the early rare-earth atoms more favorable for (partial) substitution of the lanthanum atom. In order to shed light on the stability of such quaternary MLCs, the energy difference for the following reaction was calculated through density functional theory (DFT):

$$(LaS)_{1+y}TaS_2 + (La_{0.95}Ln_{0.05})S \rightarrow (La_{0.95}Ln_{0.05})_{1+y}STaS_2 + LaS,\ y = 0.11$$

These calculations (see Figure 7) indicate that rare earth atoms like praseodymium, neodymium and others possess a partially empty 4*f* level in the Fermi level if substituted at 5 at % level in the LaS-TaS_2 lattice [30]. Therefore, irrespective of their size, they can accept the excess electrons of the lanthanum atoms in the lattice and increase the stability of the mixed rare-earth MLC and thereby also the nanotubes. Note though, that these calculations disregard the contribution of the entropy to the reaction free energy.

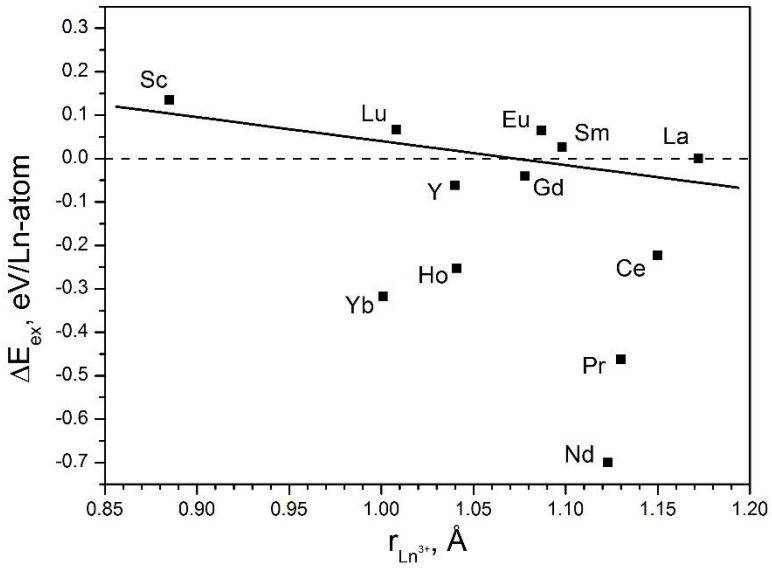


Figure 7. The energy ΔE_{ex} estimated using density functional theory (DFT) method for the exchange (5 at %) of a Ln cation between the bulk of LaS and the slab of LaS within $(LaS)_{1.11}TaS_2$ misfit compound, as a function of the Ln^{3+} cation radius r. Negative value ΔE_{ex} signifies favorable environment for the Ln dopant within the quaternary misfit lattice. The full curve indicates a trend in the variation of ΔE_{ex} as a function of the steric factor alone. However, several Ln cations with open electronic shell, which are stronger electron acceptors, like Nd, Pr etc., show negative ΔE_{ex} (courtesy of Dr. A. Enyashin).

The proportion of the rare-earth atoms (La and Ln) in the precursors was much higher than in the calculations, i.e., 50:50 [30]. The synthetic procedure was very similar to the one described above (CVT growth technique). The products were analyzed mostly through different electron microscopy techniques and Raman spectroscopy. Table 2 summarizes the results of the analysis of the quaternary $Ln_xLa_{(1-x)}S$-TaS_2 nanotubes and compares the (relative) nanotube yields to those reported for the pure LnS-TaS_2 ones (in parentheses). With the exception of holmium, the Ln atoms were present in the nanotubes' lattice in appreciable amounts. Note that, unlike the prediction of the theoretical calculations (Figure 7), the yield of the samarium-based MLC nanotubes was very high (88%).

Table 2. Yield and results of the energy dispersive X-ray spectroscopy (EDS) (TEM) quantification acquired on the $Ln_xLa_{(1-x)}S$-TaS_2 nanotubes. The yields of the pure $LnTaS_3$ tubes were taken from [24,45]. In parentheses—the yield for the pure LnS-TaS_2 nanotubes [24,45].

Sample	$LaTaS_3$ [20]	(Pr,La)TaS_3	(Sm,La)TaS_3	(Ho,La)TaS_3	(Yb,La)TaS_3
Yield (%)	50 [20,37]	55 (7) [37]	88 (59) [37]	97 (5) [37]	37 (1) [37]
Ln (at.%)	-	11.7	13.3	4.4	10.0
La (at.%)	-	7.1	8.6	21.4	13.0
Ta (at.%)	-	18.8	22.3	22.1	23.3
S (at.%)	-	62.5	55.8	51.1	53.7
Ln/(La + Ln) (%)	-	62	61	16	43

It can be concluded therefore that alloying with certain foreign atoms is a suitable strategy for increasing the stability of the MLC and nanotubes thereof. Simultaneously, nanotubes containing more than one rare-earth atom can have interesting properties, like emission in two wavelengths, tunable infrared absorption (see below), and other interesting physical properties.

2.7. MLC Nanotubes from Alloys of Yttrium and Lanthanum

MLC compounds of yttrium sulfide are rather rare. The MLC compound $(YS)_{1.23}NbS_2$ was studied before in the bulk form [46], as well as $(YS)_{1.17}VS_2$, but not its analogous compound with Ta as transition metal. Nanotubes based on the quaternary misfit layered compound $La_{1-x}Y_xS$-TaS_2 ($0 \leq x \leq 1$) were recently reported [31]. The nanotubes were synthesized using the standard chemical vapor transport technique. The yttrium replaced the lanthanum atom over the entire range, i.e., from a pure LaS-TaS_2 to YS-TaS_2. However, the yield of the nanotubes went down with increasing Y content.

Electron diffraction analysis showed that in analogy to the LaS-TaS_2 nanotubes, the ternary YS-TaS_2 nanotubes possess a single orientation vector, i.e., the *b*-axis coincided with the growth axis of the nanotubes. Thus, six pairs of diffraction spots were observed for the hexagonal lattice (TaS_2) and four pairs for the rocksalt lattice with a chiral angle of 3°. Contrarily, in the quaternary $La_{1-x}Y_xS$-TaS_2 tubes of different compositions, the *b*-axis of different layers was rotated by 30° with respect to each other. In several cases, the nanotubes exhibited double spacing (2.2 nm for the *c*-axis instead of 1.1 nm), i.e., the adjacent $Y_xLa_{1-x}S$-TaS_2 layers showed an alternating rotation of 30° with respect to each other, periodically. Double periodicity was already noticed in nanotubes of the mixed MLC compound LaS-$Nb_{0.8}Ta_{0.2}S_2$ type [28] and in some of the LnS-$TaSe_2$ tubes [29]. The $Y_xLa_{1-x}S$ sublattice and the stacking periodicity along the *c*-axis was found to decrease uniformly with increasing Y content, which goes hand in hand with the smaller lattice constant of YS compared to that of LaS. The reduction in the interlayer spacing with ascending yttrium content is indicative of a stronger interlayer interaction and larger degree of charge transfer from the MS layer to the TS_2 layer upon increasing the yttrium content. This tendency is compatible with the observation of a larger blueshift of the E_g Raman mode of the TaS_2 unit with increasing Y-content.

2H-TaS_2 is a semi-metal with a half-filled $5dz^2$ band. The intercalation of a LnS slab in the hexagonal lattice leads to a significant charge transfer from the rare-earth (Ln) atom to the half-filled $5dz^2$ band of TaS_2 and reduces the overall free carrier density in this layer. In order to shed light on this process, Fourier-transform infrared (FTIR) measurements were carried-out for powders with increasing yttrium content (see Figure 8a). The transmissivity edge was found to shift to lower wavenumbers with increasing Y-content in the MLC. This shift was attributed to the reduction in the free carrier density of the TaS_2 slab with increasing yttrium content. The Drude-Lorentz model was employed to calculate the free carrier density in the TaS_2 slab and the amount of charge transfer from the rocksalt unit to the hexagonal TaS_2 unit (Figure 8b) (see [47]). Indeed the carrier density in the TaS_2 decreased with increasing yttrium content in the MLC lattice, however not in a uniform fashion. The maximum around 20 at % yttrium content can be ascribed to a gradual structural change from a La-rich phase

$(MS)_{1.14}TaS_2$ to an yttrium-rich phase-$(MS)_{1.2}TaS_2$. This overall trend was confirmed also via Raman and STEM-EELS analysis of individual nanotubes with different Y-content.

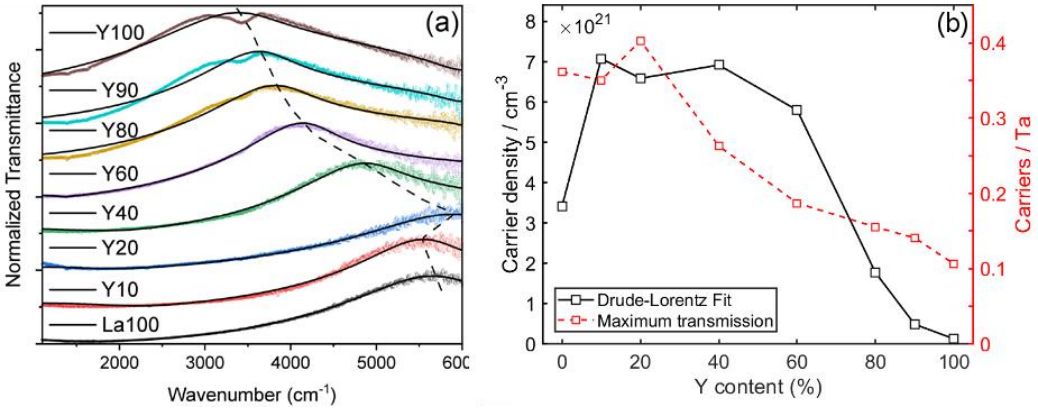


Figure 8. (**a**) Normalized transmission spectra of $(Y_xLa_{1-x})S\text{-}TaS_2$ compounds with varying proportions of yttrium (Y40 stands for $(Y_{0.4}La_{0.6})S\text{-}TaS_2$). The solid lines represent the fitted Drude-Lorentz model. The dashed line (guide to the eye) indicates the non-linear shift of the transmittance in the spectra. (**b**) The variation of the carrier density and carriers per Ta atom calculated from the Drude-Lorentz model (black curve) and separately from the maximum transmissivity model (dashed red curve) as a function of Y at % in the $(Y_xLa_{1-x})S\text{-}TaS_2$ misfit compound. Adopted from [31] with ACS permission.

DFT analysis (see Figure 7) showed that indeed the compound $Y_{0.05}La_{0.95}S\text{-}TaS_2$ possesses negative energy and hence is predicted to be a stable material. Furthermore, the $Y_xLa_{1-x}S\text{-}TaS_2$ MLC was found to be stable over the entire composition $0 \leq x \leq 1$. Moreover, the equivalent scandium compound was found to be unstable (see Figure 7). Indeed, attempts to synthesize this compound by the present CVT technique were unsuccessful, which adds credibility to the present DFT calculations. Therefore, a new series of misfit compound alloys $Y_xLa_{1-x}S\text{-}TaS_2$ with $0 \leq x \leq 1$ was reported. The tenability of the charge transfer from the rocksalt to the hexagonal unit, accomplished through controlled variation of the yttrium (and lanthanum) content, influences the electronic as well as the optical properties of this quaternary MLC.

In conclusion, the study of nanotubes of quaternary MLCs provided rich information on the relationship between the chemistry, structure, and optical properties of such nanotubes. It can be anticipated that on top of this interesting information, their physico-chemical properties, especially at low temperatures, will provide ample information and show some enticing behavior, which is out of the scope of the present study.

3. Films and Bulk Quaternary MLC

Several techniques have been described in the literature for producing films and bulk crystals of quaternary MLC alloys, which will be briefly described here.

3.1. Ferecrystals from the Modulated Elemental Reactants Technique

Prelude: The composition and structure of products obtained via high-temperature solid-state reactions, like CVT as described above, are dictated by equilibrium thermodynamics. On the other hand, the modulated elemental reactants (MER) technique was found to be a successful methodology for the syntheses of two-dimensional MLCs with complex composition, which cannot be obtained via reactions carried out under equilibrium-thermodynamic conditions. This approach was proposed by Johnson and co-workers and used for the preparation of families of related structures with sophisticated nanoarchitecture [48,49]. The mechanism of MER is based on a diffusion-constrained self-assembly of compositionally modulated amorphous precursors to form kinetically stable films. Standard deposition process of metals is carried out with a 3 kW electron beam gun and chalcogens using a Knudsen

effusion cell. In this technique, a one-atom-thick layer of each of the constituting atoms are deposited, sequentially. After a few tens of such layers have been deposited, the film is annealed at relatively modest temperatures of between 300–500 °C so as to induce a chemical reaction but avert interdiffusion of the layers. This methodology has enabled synthesis of films of many kinds of misfit (ferecrystals) compounds. Due to the low annealing temperatures, complex materials, which are metastable and do not exist in the bulk form, could be nevertheless prepared. However, turbostratic disorder in the layers cannot be fully avoided under such modest annealing conditions. Of the few works published on quaternary ferecrystal films (see Table 1), two examples are described here.

3.2. $(SnSe)_{1.16-1.09}(Nb_xMo_{1-x})Se_2$ Ferecrystal Films

An interesting aspect of quaternary ferecrystals is the ability to modulate the charge density in the hexagonal TX_2 layer via charge manipulation of the distorted rocksalt structure in the $M^{-}M^{2}{}_{1-X}X_2$ layer. This charge modulation is reminiscent of the situation in the electron gas of composition modulated quantum wells of III-V compounds, which have been investigated for longer than four decades now. Thus, by using two metal atoms, M_1 and M_2, belonging to a different column in the periodic table, the amount of charge transferred to the TX_2 layer can be modulated over several orders of magnitudes. Indeed, one important aspect of the MER technique is the possibility to control the charge carrier density by varying the M_1 to M_2 ratio over the entire composition range. This level of control does not exist in, e.g., chemical vapor transport growth, where the partition of the two metal atoms in the gas phase and in the solid can differ remarkably.

$(SnSe)_{1.16-1.09}Nb_xMo_{1-x}Se_2$ with x = 0, 0.26, 0.49, 0.83, and 1 were prepared from designed modulated precursors using the modulated elemental reactant technique in a physical vapor deposition vacuum system [32] (Figure 9). Mo and Nb were arc melted to create dense pieces of suitable size. For films made of alloys with quaternary composition, Nb and Mo were added in the desired stoichiometric amounts and then arc-melted. Metal sources were evaporated at rates of approximately 0.2 Å/s for Mo and Nb and 0.4 Å/s for Sn using 3 kW electron beam guns. Se was evaporated using a custom built Knudsen effusion cell at a rate of about 0.5 Å/s. After several repetitions, 500 to 600 Å thick film was obtained (Figure 9). The molybdenum-rich MLC phase would not be expected to be a stable MLC compound and indeed was not reported in the literature. The fact that a metastable film of these compositions could be produced is attributed to the low annealing temperatures (400 °C) of the process (Figure 9). Annealing at higher temperatures would probably lead to interdiffusion of the reactants, destruction of the superlattice structure, and demixing of the binary phases into isolated crystallites.

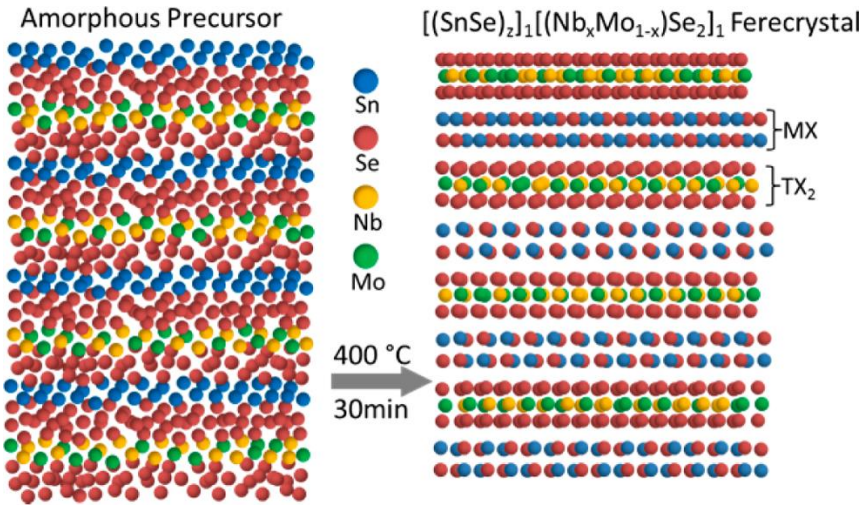


Figure 9. Schematic drawing of the synthesis of $(SnSe)_{1.09-1.16}Nb_xMo_{1-x}Se_2$ alloy ferecrystals. On the left is the as-deposited amorphous precursor. On the right is the ferecrystal alloy after annealing (400 °C) and self-assembly (adopted with permission of the ACS from [32]).

A linear decrease in the *c*-lattice parameter was observed from 12.53 Å for $(SnSe)_{1.09}MoSe_2$ to 12.27 Å for $(SnSe)_{1.16}NbSe_2$. A linear increase in the *a*-parameters of the dichalcogenide constituent was observed from 3.329 Å for $(SnSe)_{1.09}MoSe_2$ to 3.461 Å for $(SnSe)_{1.16}NbSe_2$. A slight change was also observed in the *a*-lattice parameter of the rocksalt constituent leading to a linear increase in the misfit parameter of the alloys with increased Nb content.

Temperature dependent electrical resistivity measurements showed that upon increasing the Nb content, the film transformed from a semiconductor into a metal. These measurements show that the transport properties of ferecrystal films can be controlled in an unprecedented fashion. However, the disorder in the turbostratic structure of the film leads to excessive scattering and impedes the mobility of the free carriers.

With an eye on controlling the charge density wave (CDW) transition in 1T-VSe_2, which could be useful for modulating electro-optic signals, this group reported the synthesis of $(Sn_{1-x}Bi_xSe)_{1.15}VSe_2$ films using the modulated elemental reactants technique [44,50]. Increasing the bismuth content in the ferecrystal film, the *c*-axis contracts signifying a stronger $Sn_{1-x}Bi_xSe$-VSe_2 interlayer interaction. In the pure $(SnSe)_{1.15}VSe_2$, a strong increase in resistivity was observed below around 100 K, which was attributed to a CDW transition. With just 6 at % of Bi replacing the Sn in the ferecrystal lattice, an enhancement by a factor of three was observed in this resistivity jump near 100 K compared to the original $(SnSe)_{1.15}VSe_2$. This remarkable behavior is indicative of the level of charge modulation in the 1T−VSe_2 layers by lattice substitution in the rocksalt lattice.

3.3. Bulk Quaternary MLC of Chalcogenides

Recently the synthesis of microcrystallites of two quaternary MLCs, i.e., $[(Bi_{0.4}Nd_{0.6})S]_{1.25}CrS_2$ and $[(Pb_{0.5}Nd_{0.5})Se]_{1.15}(NbSe_2)_2$, were reported [33]. The synthesis involved a two-phase reaction, the homogenization phase at 500 °C (2 h), and the MLC synthesis at 1000 °C (18 d). Many of the crystals showed curly edges, which is indicative of the strain relaxation mechanism between the M_1M_2X and TX_2 sublattices, as discussed above. The structure of the two quaternary MLCs was elucidated in great detail, but no functional characterization of these compounds has been put forward, so far.

1T−$TiSe_2$ is a layered compound with octahedral coordination between the titanium and selenium atoms. It is also known to exhibit a commensurate CDW transition at 202 K. Furthermore, when doped with copper or palladium, this compound becomes a superconductor. Copper intercalation of the homologous series $(BiSe)_{1+y}(TiSe_2)_n$ $0 \leq x_{Cu} \leq 0.1$ was undertaken in order to control the CDW transition and the superconductivity of these compounds [51]. It was found that upon copper intercalation, the integer n goes from 1 to 2 with proper lattice expansion along the *c*-axis. This interesting structural transformation implies that the copper atoms do not substitute the Bi atoms in the rocksalt lattice, but rather intercalate in the galleries between each two $TiSe_2$ layers of $(BiSe)_{1+y}(TiSe_2)_2$. The intercalation compounds with copper up to x = 0.1 loading showed metallic behavior, but did not exhibit any superconductivity transition down to 0.05 K.

3.4. Quaternary MLC Cobaltites

One of the early works on quaternary MLC cobaltites was based on the analogy with the high *Tc* cuprate superconductors, where the 2D-like oxides are spatially separated into the Cu-O slabs serving as conducting blocks and rare-earth oxide blocks (with rocksalt structure), which play the role of charge reservoirs. In this work, MLC cobaltites of the formula $Bi_2M_3Co_2O_y$ with M = Ca, Sr, Ba were prepared via the flux method [34]. In addition, Pb-doped $Bi_2M_3Co_2O_y$ where the lead atom was substituted for the bismuth sites (quintenary MLC), were also prepared. The $(Bi,Pb)_2Ba_3Co_2O_y$ exhibited metallic conductivity down to 30 mK. Quaternary multilayered cobaltites were synthesized as bulk crystals using the flux method from a mixture of Bi_2O_3, $CaCO_3$, and Co_3O_4. The reagents were annealed under a pressure of one bar argon at 600 °C, which is somewhat higher than the melting temperature of the B_2O_3 flux. Inductively-coupled plasma spectrometry revealed the composition $(Bi_2Ca_2O_4)_qCoO_2$ with a *q* value of 0.627 [35]. Similarly, Reference [52] reported the synthesis of bulk crystals of the quaternary

cobaltite-$(Bi_2Sr_2O_4)_{0.51}CoO_2$ using the same flux method. The initial reagents Bi_2O_3, $SrCO_3$, and Co_3O_4 were mixed in a molar ratio of 3:3:1 and were annealed in argon atmosphere at 600 °C for 48 h.

The resistivity of the $(Bi_2Ca_2O_4)_qCoO_2$ was measured along the *c*-axis and in the *a*-*b* plan using both *dc* and *ac* techniques as a function of temperature [35]. The resistivity above 60 K was found to be thermally activated obeying the Arrhenius rule. The ratio ρ_c/ρ_{ab} varied in the range of 50–150 demonstrating the large anisotropy, which is typical for 2D materials in general. This anisotropy is not limited, of course, to the conductivity and is characteristic of numerous physic-chemical properties of 2D materials and MLCs among them.

4. Applications

4.1. Thermoelectric Properties

The functional characterization of MLCs and quaternary MLCs in particular is rather limited, with the exception of thermoelectric power generation, which has been studied studied mostly in relation to the cobaltites. The energy conversion efficiency of thermoelectric devices is described by the figure of merit *Z*T expressed as $ZT = S^2T/\rho k$, where *S* (in μV/K) is the Seebeck coefficient, ρ is the electrical resistivity, and *k* is the total thermal conductivity including the electronic and phononic contributions. Thus, materials with a large figure of merit should possess high electrical conductivity and low thermal conductivity, which is almost counterintuitive and not easy to achieve in a single phase material. Various strategies have been described to reduce the thermal conductivity, primarily by fabricating a composite structure with a thermal barrier between the two phases. These barriers scatter the phonons effectively and reduce the thermal conductivity of the material having minor if any effect on the electrical conductivity. Therefore, the natural barrier between the rocksalt and the hexagonal layers of a misfit compound could be ideally suited for this purpose. The alternating molecular layers of, e.g., hexagonal (octahedral) CoO_2 (TiS_2) and insulating rocksalt Ca_2CoO_3 or SnS, could be ideally suited for scattering of the phonon flux without compromising the electrical current, achieving thereby high *Z*T materials.

Doping of a ternary MLC with impurity atoms was proposed as a useful strategy for further reducing the thermal diffusivity of the phonons, while having a minor or even positive effect on the electrical conductivity of the MLC. One such example is the ternary MLC $(SnS)_{1.2}(TiS_2)_2$. A conventional solid-state reaction method was used to synthesize $(SnS)_{1.2}(Co_{0.02}Ti_{0.98}S_2)_2$ (with 2 at % cobalt atoms) and substituted $(SnS)_{1.2}(Cu_{0.02}Ti_{0.98}S_2)_2$ (with 2 at % copper atoms) [36]. For the synthesis of these two quaternary MLCs, elemental Sn, Ti, S, and Cu (and Co at 2 at %) were mixed in the ratio 1:2:5 and sealed in evacuated quartz tubes. The mixture was heated at 800 °C for 48 h. The authors reported that the substitution of Co^{3+} and Cu^{2+} for Ti^{4+} ions led to quite a significant increase of the figure of merit from about 0.28 for the pristine to 0.42 for the copper doped sample at 720 K. This increment was attributed to the enhanced electrical transport properties and also to improved phonon scattering.

Much work has been devoted to the study of the thermoelectric effect in the cobaltite MLC and more recently to those made of four elements [53]. In one such study, a family of misfit cobaltites $(Bi_2A_2O_4)_qCoO_2$ (A = Ca, Sr, and Ba, $0.505 \leq q \leq 0.592$), with the acronyms BCCO, BSCO, and BBCO, respectively, was investigated [53]. The value of $q = b_2/b_1$ is determined by the ratio between the *b*−axis of the rocksalt unit (b_1) and that of the CoO_2 (b_2). Since all the rare-earth atoms studied had the same valency (+2), the amount of the charge transfer between the rocksalt and hexagonal CoO_2 units was attributed to a geometrical factor and determined by the value of *q*. The smaller the value of *q* (in Ba) the higher is the charge density and conductivity in the metallic (doped) CoO_2 layer, which was confirmed by resistivity and Hall effect measurements. Figure 10 shows the in-plane Seebeck coefficient- *S* as a function of temperature for each of the quaternary cobaltites. All three functions *S*(T) demonstrate the same behavior: they exhibit metallic-like ($dS/dT > 0$) behavior at low temperatures. However, at T > 200 K a plateau with a small T dependence is reached. The magnitude of *S* for BBCO, BSCO, and BCCO is 94, 123, and 149 μVK^{-1} at 320 K, respectively. The size of the A atoms in $(Bi_2A_2O_4)_qCoO_2$ determine

the charge transfer between the block layers. Therefore, reduction in q (Ba^{2+} instead of Ca^{2+}) induces an increase of the formal Co valency, i.e., higher fraction of Co^{4+} in the CoO_2 layer. Since the Seebeck coefficient goes down and the resistivity increases by replacing calcium with barium, the overall figure of merit ZT remains almost the same across the rare-earth series of this compound at 320 K.

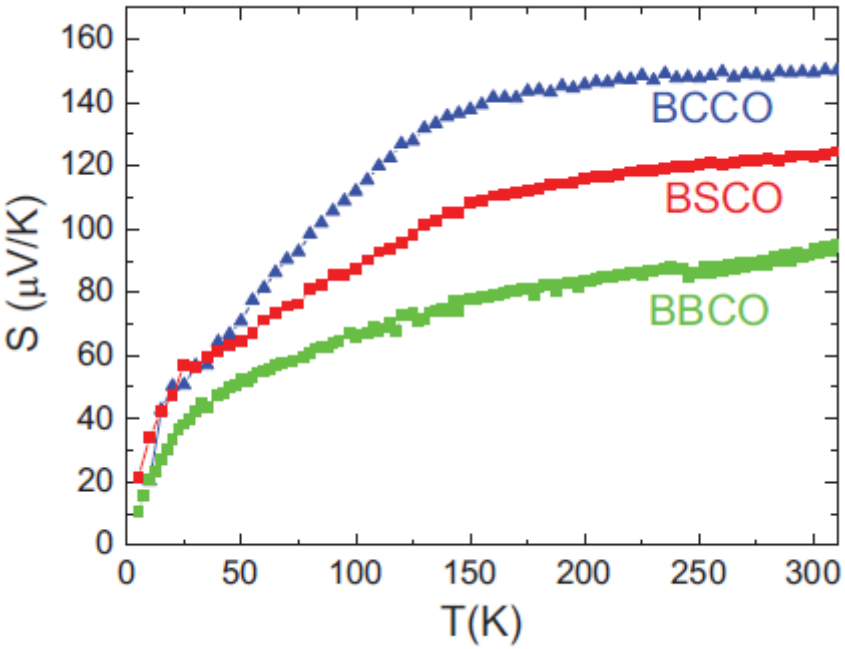


Figure 10. In-plane thermopower S for BBCO, BSCO, and BCCO single crystals (adopted with permission from Wiley−VCH from Reference [53]).

In conclusion, the doped MLCs of the cobaltites are an interesting class of thermoelectric materials. Their electrical and thermal properties as well as their thermoelectric power can be tuned by both size and valency effects of the dopant ions.

4.2. Rechargeable Ca-Ion Batteries

Preliminary theoretical and experimental work on cathode materials of layered cobaltites for Ca-ion rechargeable batteries was recently presented [54]. The authors studied several calcium-cobalt oxide compounds, including layered $CaCo_2O_4$ and the MLC $(Ca_2CoO_3)_{0.618}CoO_2$. The combined theoretical−experimental work found that among the different cobaltites studied in this work the layered $CaCo_2O_4$ present the thermodynamically smallest diffusion barrier for calcium intercalation and also the fastest diffusion kinetics for such an electrode. However, given the fact that this is the first study of its kind, there is a lot of room for research in this direction, including MLCs made of quaternary cobaltites, which have not been investigated in this context so far.

4.3. Electronic and Optoelectronics Properties

Quite a few MLCs, like $(PbS)_{1.13}TaS_2$, $(BiS)_{1.07}TaS_2$ [55], and $(LaSe)_{1.14}NbSe_2$ [56], exhibit superconducting transition at low temperatures. Modulation of the carrier density in the MLC lattice is of great importance for controlling the superconducting transition. In general, however, the critical temperature T_c is lower for the MLC (1.32 K for $(LaSe)_{1.14}NbSe_2$) compared to that of the pure hexagonal compound, like $NbSe_2$ (7.2 K) [56].

The structure and transport properties of the quaternary MLC of the type franckeite $[(Pb,Sb)S]_{2.28}NbS_2$ were studied before [55,57]. Interestingly, the T_c of this compound (1.05 K) is lower than that of ternary $(PbS)_{1.14}NbS_2$ (2.6 K) and appreciably lower than that of pure NbS_2 (6.2 K). This trend is attributed to the lower number of the metallic NbS_2 slabs in the unit cell of the MLC [57].

If one considers the mean oxidation state of niobium, it goes down from the formal +4 in NbS_2 to a value between +3 and +4 in the MLC compounds, due to a partial charge transfer from the distorted cubic slabs. The smaller valency of the niobium leads to a reduced carrier density in the NbS_2 slab.

The dynamics of the CDW transition of 1T-TaS_2 has been studied in the past as a means for optoelectronic switching and for optical data storage devices [58]. The non-trivial topology of the CDW state across the layers in the 3D structure is a topic of current debate. The linkage between adjacent layers makes this state very sensitive to different kinds of defects. One motivation for the search of CDW states in MLCs, is the possibility to confine the CDW state in a single TaS_2 layer with adjacent MS layers separating it from the rest of the TaS_2 layers. Therefore, having the CDW state confined in a 2D molecular slab could offer a better means to increase the robustness of this transition. Furthermore, the tunability of the MLC with respect to doping or alloying with a foreign atom in a quaternary MLC, as discussed above, would allow the free carrier density in the TaS_2 layer to be manipulated, thereby influencing the CDW transition.

4.4. Electrochemistry and Catalysis

There is quite an extensive literature on metal intercalation into different misfit compounds, with potential applications for energy storage, 2D metallic films, and hydrogen/oxygen generation. Exfoliation of 2D materials has been studied extensively in recent years with prime interest in energy conversion and storage devices. Regardless of the specific 2D material, the large surface area and the elimination of bottlenecks in the electrodes made of exfoliated sheets, like diffusion controlled reactions and slow intercalation, played a primordial role in improving the power density and increasing the lifetimes of such devices. Not surprisingly therefore, the potential of exfoliated films in the limit of a single molecular MLC slab has received some attention in recent years. An early example is the sodium and lithium intercalation in the PbS-NbS_2 and PbS-$(NbS_2)_2$ MLC electrodes in the Na/Na-perchlorate-propylene carbonate/sulfide electrochemical cells [37]. Remarkably, the PbS-NbS_2 electrode was stable only for a very limited sodium uptake, while the second MLC was stable up to 0.9 at/mol of sodium. This stability was attributed to the intercalation of the sodium ions in the octahedral sites of the NbS_2-NbS_2 gap of the PbS-$(NbS_2)_2$ MLC. Not unexpectedly, the sodium intercalation led to a significant expansion of the lattice in the *c*-direction. In the absence of a van der Waals gap in PbS-NbS_2, sodium insertion into this material becomes a non-reversible reaction making this electrode highly unstable.

In a more recent work, bulk quaternary MLC $Bi_2Sr_2Co_2O_{8+\delta}$ (SrO-BiO-BiO-SrO-CoO_2) and their exfoliated nanosheets were prepared and tested as electrodes for the oxygen evolution reaction [38]. The substantially higher reactivity of the electrode made of exfoliated single slab MLC was attributed to the large surface area and the high spin states of the Co^{3+} atoms at the edges of the nanosheets. In yet another work, the hydrogen evolution reaction was studied with an electrode made of exfoliated $Bi_{1.85}Sr_2Co_{1.85}O_{7.7-\delta}$ (SrO-BiO-BiO-SrO-CoO_2) MLC [59]. The performance of this specific electrode was found to be largely inferior to those made of precious metal electrodes. Nonetheless, the authors concluded that the interplay between the complex chemistry of MLC and their electrochemical reactivity in energy conversion reactions is worth further exploration.

4.5. Concluding Remarks

Misfit layered compounds (MLCs) have been investigated for almost 50 years now. Initially, their research focused on the study of the detailed structure of naturally occurring minerals, like franckeites. As of the last decade of the previous century, extensive synthetic effort resulted in the discovery of numerous new families of MLCs, and their physical properties were studied to a certain extent. The electronic structure of MLC has not been investigated thoroughly so far, due largely to the complex structure (irrational numbers) of MLCs, which forced researchers to use large unit cells to simulate "approximants" with well-defined, but approximated, unit cells. This situation is further exacerbated for quaternary MLCs where the distribution of the different elements on the same sublattice of the

approximant is unknown a priory. With the advent of density functional theory algorithms, the electronic structure and many of the MLC properties can be calculated systematically now. In recent years, the search for synthetic MLCs with larger than three elements has advanced considerably. Adding a new element on the same sublattice provides a new gauge for controlling the free carrier density and thereby the electronic, magnetic, and optical properties as well as the chemical reactivity of quaternary MLCs. As of the beginning of the new millennium, nanostructures, like MLC nanotubes, were prepared satisfactorily for the first time. Moreover, exfoliating MLCs, leading to single layer nanostructures of different ternary and later quaternary MLCs, have been prepared. These developments open a vast field for research, which is likely to expand in the future. Heterostructures, made of a stacking of different 2D materials with MLC monolayers included, can be envisioned for engineering of new electronic devices. Catalysis and energy conversion and storage devices can also greatly benefit from these new directions. Coupled with their broad chemical versatility, and with different applications in mind for energy conversion and storage devices and for optoelectronics, this large group of materials could potentially become a playground for vast future research and a plethora of applications.

Author Contributions: S.B.A. (Y.E.) methodology, investigation, writing; R.T. Conceptualization, validation, supervision, writing. All authors have read and agreed to the published version of the manuscript.

Funding: This work was partially supported by the Israel Science Foundation No. 339/18 Grant No. 120924, the Sustainability and Energy Research Initiative (SAERI) of the Weizmann Institute (Grant No. 7220730101), the Perlman Family Foundation, and the Kimmel Center for Nanoscale Science Grant No. 43535000350000.

Conflicts of Interest: The authors declare no conflict of interest.

References

1. Lorenz, T.; Joswig, J.; Seifert, G. Two−dimensional and tubular structures of misfit compounds: Structural and electronic properties. *Beilstein J. Nanotechnol.* **2014**, *5*, 2171–2178. [CrossRef]
2. Panchakarla, L.S.; Radovsky, G.; Houben, L.; Popovitz-Biro, R.; Dunin-Borkowski, R.E.; Tenne, R. Nanotubes from Misfit Layered Compounds: A New Family of Materials with Low Dimensionality. *J. Phys. Chem. Lett.* **2014**, *5*, 3724–3736. [CrossRef]
3. Wiegers, G.A. Misfit Layered Compounds: Structures and Physical Properties. *Prog. Solid State Chem.* **1996**, *24*, 1–139. [CrossRef]
4. Makovicky, E.; Hyde, B.G. Non-Commensurate (Misfit) Layer Structures. In *Inorganic Chemistry; Structure and Bonding*; Series Springer: Heidelberg, Germany, 1981; Volume 46, p. 101.
5. Wiegers, G.A.; Meerschaut, A. Incommensurate Sandwiched Layered Compounds. In *Materials Science Forum*; Meerschaut, A., Ed.; Trans Tech Publications: Pfaffikon, Switzerland, 1992; Volume 100–101, pp. 101–172.
6. Gómez-Herrero, A.; Landa-Cánovas, A.R.; Hansen, S.; Otero-Díaz, L.C. Electron Microscopy Study of Tubular Crystals $(BiS)_{1+\delta}(NbS_2)_n$. *Micron* **2000**, *31*, 587–595. [CrossRef]
7. Spiecker, E.; Garbrecht, M.; Jäger, W.; Tillmann, K. Advantages of Aberration Correction for HRTEM Investigation of Complex Layer Compounds. *J. Microsc.* **2010**, *237*, 341–346. [CrossRef] [PubMed]
8. Bernaerts, D.; Amelinckx, S.; Van Tendeloo, G.; Van Landuyt, J. Microstructure and Formation Mechanism of Cylindrical and Conical Scrolls of the Misfit Layer Compounds $PbNb_nS_{2n+1}$. *J. Cryst. Growth* **1997**, *172*, 433–439. [CrossRef]
9. Kato, K.; Kawada, I.; Takahashi, T. Die Kristallstruktur von $LaCrS_3$. *Acta Cryst. B* **1977**, *33*, 3437–3443. [CrossRef]
10. Boullay, P.; Domengès, B.; Hervieu, M.; Groult, D.; Raveau, B. Evidence for the First Misfit Layer Oxide $Tl_{0.41}(Sr_{0.9}O)_{1.12}CoO_2$. *Chem. Mater.* **1996**, *8*, 1482–1489. [CrossRef]
11. Miyazaki, Y.; Kudo, K.; Akoshima, M.; Ono, Y.; Koike, Y.; Kajitani, T. Low-Temperature Thermoelectric Properties of the Composite Crystal $[Ca_2CoO_{3.34}]_{0.614}[CoO_2]$. *Jpn. J. Appl. Phys.* **2000**, *39*, L531–L533. [CrossRef]
12. Karppinen, M.; Fjellvag, H.; Konno, T.; Morita, Y.; Motohashi, T.; Yamauchi, H. Evidence for Oxygen Vacancies in Misfit-Layered Calcium Cobalt Oxide, $[CoCa_2O_3]_qCoO_2$. *Chem. Mater.* **2004**, *16*, 2790–2793. [CrossRef]

13. Panchakarla, L.S.; Lajaunie, L.; Ramasubramaniam, A.; Arenal, R.; Tenne, R. Nanotubes from Oxide-Based Misfit Family: The Case of Calcium Cobalt Oxide. *ACS Nano* **2016**, *10*, 6248–6256. [CrossRef]
14. Limelette, P.; Hebert, S.; Hardy, V.; Frésard, R.; Simon, C.; Maignan, A. Scaling Behavior in Thermoelectric Misfit Cobalt Oxides. *Phys. Rev. Lett.* **2006**, *97*, 046601–046605. [CrossRef]
15. Butt, S.; Liu, Y.-C.; Lan, J.-L.; Shehzad, K.; Zhan, B.; Lin, Y.; Nan, C.-W. High−Temperature Thermoelectric Properties of La and Fe Co-Doped Ca-Co-O Misfit-Layered Cobaltites Consolidated by Spark Plasma Sintering. *J. Alloys Compd.* **2014**, *588*, 277–283. [CrossRef]
16. Henriksen, R.B.; Makovicky, E.; Stipp, S.L.S.; Nissen, C.; Eggleston, C.M. Atomic-Scale Observations of Franckeite Surface Morphology. *Am. Mineral.* **2002**, *87*, 1273–1278. [CrossRef]
17. Bengel, H.; Jobic, S.; Moëlo, Y.; Lafond, A.; Rouxel, J.; Seo, D.-K.; Whangbo, M.-H. Distribution of the Pb and Sb Atoms in the (Pb,Sb)S Layers of the Franckeite-Type Misfit Compound $[(Pb, Sb)S]_{2.28}NbS_2$ Examined by Scanning Tunneling and Atomic Force Microscopy. *J. Solid State Chem.* **2000**, *149*, 370–377. [CrossRef]
18. Tenne, R.; Margulis, L.; Genut, M.; Hodes, G. Polyhedral and cylindrical structures of tungsten disulphide. *Nature* **1992**, *360*, 444–446. [CrossRef]
19. Margulis, L.; Salitra, G.; Tenne, R.; Talianker, M. Nested Fullerene-Like Structures. *Nature* **1993**, *365*, 113–114. [CrossRef]
20. Feldman, Y.; Wasserman, E.; Srolovitz, D.J.; Tenne, R. High-Rate, Gas-Phase Growth of MoS_2 Nested Inorganic Fullerenes and Nanotubes. *Science* **1995**, *267*, 222–225. [CrossRef]
21. Hong, S.Y.; Popovitz-Biro, R.; Prior, Y.; Tenne, R. Synthesis of SnS_2/SnS Fullerene-Like Nanoparticles: A Superlattice with Polyhedral Shape. *J. Am. Chem. Soc.* **2003**, *125*, 10470–10474. [CrossRef]
22. Radovsky, G.; Popovitz-Biro, R.; Staiger, M.; Gartsman, K.; Thomsen, C.; Lorenz, T.; Seifert, G.; Tenne, R. Synthesis of Copious Amounts of SnS_2 and SnS_2/SnS Nanotubes with Ordered Superstructures. *Angew. Chem. Int. Ed.* **2020**, *50*, 12316–12320. [CrossRef]
23. Ohno, Y. Lamellar and Filament-Like Crystals of Misfit-Layer Compounds Containing (Sm, Ta, S) and (Pb, Bi, Nb, S) Elements. *J. Solid State Chem.* **2005**, *178*, 1539–1550. [CrossRef]
24. Radovsky, G.; Popovitz-Biro, R.; Lorenz, T.; Joswig, J.-O.; Seifert, G.; Houben, L.; Dunin-Borkowski, R.E.; Tenne, R. Tubular structures from the LnS-TaS_2 (Ln = La, Ce, Nd, Ho, Er) and LaSe-$TaSe_2$ misfit layered compounds. *J. Mater. Chem. C* **2016**, *4*, 89–98. [CrossRef]
25. Cario, L.; Johrendt, D.; Lafond, A.; Felser, C.; Meerschaut, A.; Rouxel, J. Stability and Charge Transfer in the Misfit Compound $(LaS)(SrS)_{0.2}CrS_2$: Ab Initio Band-Structure Calculations. *Phys. Rev. B* **1997**, *55*, 9409–9414. [CrossRef]
26. Nishikawa, T.; Yasui, Y.; Kobayashi, Y.; Sato, M. Studies of the Metal-Insulator Transition of Misfit-Layer Compounds $La_{1.17-x}Sr_xVS_{3.17}$. *Phys. C Supercond.* **1996**, *263*, 554–557. [CrossRef]
27. Serra, M.; Anumol, E.A.; Stolovas, D.; Pinkas, I.; Joselevich, E.; Tenne, R.; Enyashin, A.; Deepak, F.L. Synthesis and Characterization of Quaternary La(Sr)STaS_2 Misfit-Layered Nanotubes. *Beilstein J. Nanotechnol.* **2019**, *10*, 1112–1124. [CrossRef]
28. Stolovas, D.; Serra, M.; Popovitz-Biro, R.; Pinkas, I.; Houben, L.; Calvino, J.J.; Joselevich, E.; Tenne, R.; Arenal, R.; Lajaunie, L. Nanotubes from the Misfit Compound Alloy LaS-NbxTa$_{(1-x)}S_2$. *Chem. Mater.* **2018**, *30*, 8829–8842. [CrossRef]
29. Lajaunie, L.; Radovsky, G.; Tenne, R.; Arenal, R. Quaternary Chalcogenide-Based Misfit Nanotubes LnS(Se)-Ta$S(Se)_2$ (Ln = La, Ce, Nd, and Ho): Synthesis and Atomic Structural Studies. *Inorg. Chem.* **2017**, *57*, 747–753. [CrossRef]
30. Serra, M.; Lajaunie, L.; Sreedhara, M.B.; Miroshnikov, Y.; Pinkas, I.; Calvino, J.J.; Enyashin, A.N.; Tenne, R. Quaternary $Ln_xLa_{(1-x)}$S-TaS_2 Nanotubes (Ln = Pr, Sm, Ho, and Yb) as a Vehicle for Improving the yield of misfit Nanotubes. *Appl. Mater. Today* **2020**, *19*, 100581. [CrossRef]
31. Hettler, S.; Sreedhara, M.B.; Serra, M.; Popovitz-Biro, R.; Pinkas, I.; Enyashin, A.N.; Tenne, R.; Arenal, R. YS-TaS_2 and $La_{1-x}Y_xS$-TaS_2 ($0 \le x \le 1$) Nanotubes: A New Family of Misfit Layered Compounds. *ACS Nano* **2020**. [CrossRef] [PubMed]
32. Westover, R.D.; Atkins, R.A.; Ditto, J.J.; Johnson, D.C. Synthesis of $[(SnSe)_{1.16-1.09}]_1[(Nb_xMo_{1-x})Se_2]_1$ Ferecrystal Alloys. *Chem. Mater.* **2014**, *26*, 3443–3449. [CrossRef]
33. Varadé-López, R.; Gómez-Herrero, A.; Ávila-Brande, D.; Otero-Díaz, L.C. Synthesis and Electron Microscopy Study of the Quaternary Misfit Layer Chalcogenides (Bi,Nd)$S_{1+\delta}CrS_2$ and (Pb,Nd)$Se_{1+\delta}(NbSe_2)_2$. *Inorg. Chem.* **2020**, *59*, 4508–4516. [CrossRef] [PubMed]

34. Loureiro, S.M.; Young, D.P.; Cava, R.J.; Jin, R.; Liu, Y.; Bordet, P.; Qin, Y.; Zandbergen, H.; Godinho, M.; Núñez-Regueiro, M.; et al. Enhancement of metallic behavior in bismuth cobaltates through lead doping. *Phys. Rev. B* **2001**, *63*, 094109–0941013. [CrossRef]
35. Maki, M.; Machida, K.-I.; Mori, T.; Nishizaki, T.; Kobayashi, N. In-plane conduction and c-axis polarization in the misfit-layered oxide $[Bi_2Ca_2O_4]_qCoO_2$. *Phys. Rev. B* **2008**, *78*, 073101–073106. [CrossRef]
36. Yin, C.; Hu, Q.; Tang, M.; Liu, H.; Chen, Z.; Wang, Z.; Ang, R. Boosting the thermoelectric performance of misfit−layered $(SnS)_{1.2}(TiS_2)_2$ by a Co- and Cu-substituted alloying effect. *J. Mater. Chem. A* **2018**, *6*, 22909–22914. [CrossRef]
37. Hernan, L.; Morales, J.; Sanchez, L.; Tirado, J.L. Electrochemical Intercalation of Sodium into $PbNbS_3$ and $PbNb_2S_5$ Misfit Layer Compounds. *Solid State Ion.* **1992**, *58*, 179–184. [CrossRef]
38. Miao, X.; Zhou, S.; Wu, L.; Zhao, J.; Shi, L. Spin-State Transition Enhanced Oxygen Evolving Activity in Misfit-Layered Cobalt Oxide Nanosheets. *ACS Sustain. Chem. Eng.* **2018**, *6*, 12337–12342. [CrossRef]
39. Wiegers, G.A.; Meetsma, A.; van Smaalen, S.; Haange, R.J.; Wulff, J.; Zeinstra, T.; de Boer, J.L.; Kuypers, S.; Van Tendeloo, G.; Van Landuyt, J.; et al. Misfit Layer Compounds $(MS)_nTS_2$ (M = Sn, Pb, Bi, Rare Earth Elements; T = Nb, Ta; n = 1.08–1.19), a New Class of Layer Compounds. *Solid State Commun.* **1989**, *70*, 409–413. [CrossRef]
40. Svetin, D.; Vaskivskyi, I.; Brazovskii, S.; Mihailovic, D. Three-dimensional resistivity and switching between correlated electronic states in 1T-TaS_2. *Sci. Rep.* **2017**, *7*, 46048–46052. [CrossRef]
41. Kisoda, K.; Hangyo, M.; Nakashima, S.; Suzuki, K.; Enoki, T.; Ohno, Y. Raman scattering from misfit layer compounds $(RS)_xTaS_2$(R identical to La,Ce,Sm or Gd; S identical to sulphur; x approximately = 1.2). *J. Phys. Condens. Matter.* **1995**, *7*, 5383–5393. [CrossRef]
42. Karecki, D.R.; Clayman, B.P. Lattice modes and charge density waves in 1T-TaS_2. *Solid State Commun.* **1976**, *19*, 479–481. [CrossRef]
43. Radovsky, G.; Popovitz-Biro, R.; Tenne, R. Nanotubes from the Misfit Layered Compounds MS-TaS_2, where M= Pb, Sn, Sb and Bi: Synthesis and Study of their Structure. *Chem. Mater.* **2014**, *26*, 3757–3770. [CrossRef]
44. Radovsky, G.; Popovitz-Biro, R.; Stroppa, D.G.; Houben, L.; Tenne, R. Nanotubes from Chalcogenide Misfit Compounds: Sn-S, Nb-Pb-S. *Acc. Chem. Res.* **2014**, *47*, 406–416. [CrossRef] [PubMed]
45. Serra, M.; Stolovas, D.; Houben, L.; Popovitz-Biro, R.; Pinkas, I.; Kampmann, F.; Maultzsch, J.; Joselevich, E.; Tenne, R. Synthesis and Characterization of Nanotubes from Misfit $(LnS)_{(1+y)}TaS_2$ (Ln = Pr, Sm, Gd, Yb) Compounds. *Chem. Eur. J.* **2018**, *24*, 11354–11363. [CrossRef]
46. Rabu, P.; Meerschaut, A.; Rouxel, J.; Wiegers, G.A. The Crystal Structure of the Misfit Layer Compound $(YS)_{1.23}NbS_2$. *J. Solid State Chem.* **1990**, *88*, 451–458. [CrossRef]
47. Hangyo, M.; Nishio, T.; Nakashima, S.-I.; Ohno, Y.; Terashima, T.; Kojima, N. Raman and Infrared Spectra of Misfit Layer Compounds $MNbS_3$ (M = Sn, Pb, La, Ce). *Jpn. J. Appl. Phys.* **1993**, *32*, 581–583. [CrossRef]
48. Merrill, D.R.; Sutherland, D.R.; Ditto, J.; Bauers, S.R.; Falmbigl, M.; Medlin, D.L.; Johnson, D.C. Kinetically Controlled Site−Specific Substitutions in Higher-Order Heterostructures. *Chem. Mater.* **2015**, *27*, 4066–4072. [CrossRef]
49. Westover, R.D.; Ditto, J.; Falmbigl, M.; Hay, Z.L.; Johnson, D.C. Synthesis and Characterization of Quaternary Monolayer Thick $MoSe_2$/SnSe/$NbSe_2$/SnSe Heterojunction Superlattices. *Chem. Mater.* **2015**, *27*, 6411–6417. [CrossRef]
50. Falmbigl, M.; Hay, Z.; Ditto, J.; Mitchson, G.; Johnson, D.C. Modifying a Charge Density Wave Transition by Modulation Doping: Ferecrystalline Compounds $(Sn_{1-x}Bi_xSe)_{1.15}VSe_2$ with $0 \leq x \leq 0.66$. *J. Mater. Chem. C* **2015**, *3*, 12308–12315. [CrossRef]
51. Benjamin, A.; Trump, B.A.; Livi, K.J.T.; McQueen, T.M. The New Misfit Compound $(BiSe)_{1.15}(TiSe_2)_2$ and the Role of Dimensionality in the $Cu_x(BiSe)_{1+\delta}(TiSe_2)_n$ Series. *J. Solid State Chem.* **2014**, *209*, 6–12.
52. Maki, M.; Takakura, S.-I.; Nishizaki, T.; Ichikawa, F. Microscopic adjustment of misfit strain and charge segregation in $[Bi_2Sr_2O_4]_{0.51}CoO_2$. *Phys. Rev. B* **2015**, *92*, 165117. [CrossRef]
53. Hebert, S.; Kobayashi, W.; Muguerra, H.; Brȟard, Y.; Raghavendra, N.; Gascoin, F.; Guilmeau, E.; Maignan, A. From oxides to selenides and sulfides: The richness of the CdI_2 type crystallographic structure for thermoelectric properties. *Phys. Status Solidi B* **2012**, *210*, 69–81. [CrossRef]
54. Park, H.; Cui, Y.; Kim, S.; Vaughey, J.T.; Zapol, P. Ca Cobaltites as Potential Cathode Materials for Rechargeable Ca-Ion Batteries: Theory and Experiment. *J. Phys. Chem. C* **2020**, *124*, 5902–5909. [CrossRef]

55. Wiegers, G.A.; Meerschaut, A. Misfit Layer Compounds $(MS)_nTS_2$ (M = Sn, Pb, Bi, Rare Earth Metals; T = Nb, Ta, Ti, V, Cr; 1.08 < n < 1.23): Structures and Physical Properties, Meerschaut, A. (Ed.). *Mater. Sci. Forum* **1992**, *100–101*, 101–172.
56. Nader, A.; Lafond, A.; Briggs, A.; Meerschaut, A.; Roesky, R. Structural Characterization and Superconductivity in the Misfit Layer Compound $(LaSe)_{1.14}NbSe_2$. *Synth. Met.* **1998**, *97*, 147–150. [CrossRef]
57. Lafond, L.; Nader, A.; Moëlo, Y.; Meerschaut, A.; Briggs, A.; Perrin, S.; Monceau, R.; Rouxel, J. X-Ray Structure Determination and Superconductivity of a New Layered Misfit Compound with a Franckeite-Like Stacking, $[(Pb,Sb)S]_{2.28}NbS_2$. *J. Alloys Compd.* **1997**, *261*, 114–122. [CrossRef]
58. Vaskivskyi, I.; Gospodaric, J.; Brazovskii, S.; Svetin, D.; Sutar, P.; Goreshnik, E.; Mihailovic, I.A.; Mertelj, T.; Mihailovic, D. Controlling the Metal-to-Insulator Relaxation of the Metastable Hidden Quantum State in 1T-TaS_2. *Sci. Adv.* **2015**, *1*, e1500168. [CrossRef] [PubMed]
59. Chua, C.K.; Sofer, Z.; Jankovsky, O.; Pumera, M. Misfit-Layered $Bi_{1.85}Sr_2Co_{1.85}O_{7.7-\delta}$ for the Hydrogen Evolution Reaction: Beyond van der Waals Heterostructures. *ChemPhysChem* **2015**, *16*, 769–774. [CrossRef]



© 2020 by the authors. Licensee MDPI, Basel, Switzerland. This article is an open access article distributed under the terms and conditions of the Creative Commons Attribution (CC BY) license (http://creativecommons.org/licenses/by/4.0/).